Check for updates

JGR Atmospheres

RESEARCH ARTICLE
10.1029/2025JD043891

Atmospheric Rivers in the Iberian Peninsula: Connection With Extratropical Fronts and Precipitation

Diogo Luís[1,2], Carla Gama[1], Cátia Gonçalves[1], José M. Castanheira[3], Alexandre M. Ramos[4], Michael Sprenger[5], and Irina V. Gorodetskaya[2]

[1]Centre for Environmental and Marine Studies (CESAM), Department of Environment and Planning, University of Aveiro, Aveiro, Portugal, [2]CIIMAR – Interdisciplinary Centre of Marine and Environmental Research, University of Porto, Matosinhos, Portugal, [3]Centre for Environmental and Marine Studies (CESAM), Department of Physics, University of Aveiro, Aveiro, Portugal, [4]Institute of Meteorology and Climate Research, Karlsruhe Institute of Technology, Karlsruhe, Germany, [5]ETHZ, Zurich, Switzerland

Special Collection:
Climate and weather extremes in a warming climate: Processes, Prediction and Projection

Key Points:

- The Iberian Peninsula was affected by an annual average of 13.8 persistent (lasting at least 18 hr) atmospheric rivers (ARs) in 1979–2020
- The relationship between ARs and extratropical fronts is stronger for cold fronts than for warm fronts
- Persistent ARs are responsible for up to 30% of the annual precipitation in the northwestern region of the Iberian Peninsula

Supporting Information:

Supporting Information may be found in the online version of this article.

Correspondence to:

D. Luís and I. V. Gorodetskaya,
diogo.luis9@ua.pt;
irinag@ciimar.up.pt

Citation:

Luís, D., Gama, C., Gonçalves, C., Castanheira, J. M., Ramos, A. M., Sprenger, M., & Gorodetskaya, I. V. (2025). Atmospheric rivers in the Iberian Peninsula: Connection with extratropical fronts and precipitation. *Journal of Geophysical Research: Atmospheres*, *130*, e2025JD043891. https://doi.org/10.1029/2025JD043891

Received 3 APR 2025
Accepted 17 OCT 2025

Author Contributions:

Conceptualization: Carla Gama, José M. Castanheira, Irina V. Gorodetskaya
Data curation: Diogo Luís, Carla Gama, Irina V. Gorodetskaya
Formal analysis: Diogo Luís, Carla Gama, Cátia Gonçalves, Irina V. Gorodetskaya
Funding acquisition: Carla Gama, Irina V. Gorodetskaya

Abstract Precipitation over the Iberian Peninsula (IP) is highly sensitive to atmospheric rivers (ARs)—long corridors of anomalous horizontal and poleward moisture transport from lower latitudes. This study aims to deepen the understanding of the mechanisms behind Iberian ARs and to quantify their contribution to precipitation over a long-term period. We identify ARs affecting the IP in the ERA5 reanalysis with a 31-km horizontal resolution and covering a 42-year period (1979–2020). Additionally, we explore their association with the fronts of extratropical cyclones. Impact on IP precipitation is evaluated using regional observational gridded products (E-OBS, IB01) and global reanalysis (ERA5). Three AR events (unnamed storm in October 1979, Storm Gong in January 2013, and Storm Ana in December 2017) were selected as case studies and analyzed in detail. During 1979–2020, the IP was affected by 580 persistent ARs (lasting at least 18 hr) with an annual mean of 13.8 ± 2.8 ARs and the northern IP coast being the most affected region. The year 2013 is marked by the highest total number of persistent ARs (20). Cold fronts were found more often in the vicinity of ARs than warm fronts. Case studies highlight changes in the relationship between ARs and fronts throughout their lifecycle. Precipitation associated with persistent ARs exhibits a strong north-south gradient in the western IP with the highest contribution to annual precipitation occurring in the northern region (~30%). Our study demonstrates the important role of ARs in the Iberian precipitation using the latest high-resolution reanalysis and observational data.

Plain Language Summary Atmospheric rivers (ARs) are long corridors of strong water vapor transport that can cause heavy rain and snow when they reach land. In this study, we investigate the ARs affecting the Iberian Peninsula and quantify their contribution to total precipitation in this region. We have identified 580 ARs that affected the Iberian Peninsula between 1979 and 2020 (~14 ARs per year). These ARs are more often associated with cold fronts than warm fronts. We find that ARs are responsible for up to 30% of the precipitation in some areas of the Iberian Peninsula. This study highlights the importance of ARs for water availability in the Iberian Peninsula and advances our knowledge of the processes behind Iberian ARs.

1. Introduction

Precipitation in the Iberian Peninsula (IP) is characterized by great spatial, seasonal, and interannual variability (Cardoso Pereira et al., 2019; Parracho et al., 2016). The IP position in relation to the Atlantic Ocean and the Mediterranean Sea as well as its orographic structure are decisive for the predominant climate in this region, which is classified as Mediterranean in the south and in the east and oceanic temperate in the north (Andrade & Corte-Real, 2017). Summer rainfall is caused by convective storms triggered by local factors such as soil heating, high moisture content, and atmospheric instability (Serrano et al., 1999). Most of the IP precipitation occurs, however, between October and May especially across western Iberia and mountainous areas, and it is influenced by the North Atlantic winter storm track and accompanying frontal systems (Trigo et al., 2004, 2008). Many storms, described previously in literature, have affected the IP with large socioeconomic impacts associated with extreme precipitation events and strong winds, such as Klaus (January 2009), Xynthia (February 2010), Stephanie (February 2014), Ophelia (October 2017), Emma (March 2018), and Daniel (December 2019) (Liberato et al., 2011, 2013; Stewart, 2018; Stojanovic et al., 2021) among many others. Events like Gong (January 2013), Ana (December 2017), Elsa and Fabien (December 2019), and Filomena (January 2021) were also associated with

Investigation: Diogo Luís, Carla Gama, Cátia Gonçalves, José M. Castanheira, Irina V. Gorodetskaya
Methodology: Carla Gama, José M. Castanheira, Alexandre M. Ramos, Michael Sprenger, Irina V. Gorodetskaya
Software: Diogo Luís, Carla Gama, Cátia Gonçalves, José M. Castanheira, Alexandre M. Ramos, Michael Sprenger, Irina V. Gorodetskaya
Supervision: Carla Gama, Irina V. Gorodetskaya
Visualization: Diogo Luís, Carla Gama, Cátia Gonçalves, Irina V. Gorodetskaya
Writing – original draft: Diogo Luís, Carla Gama, Cátia Gonçalves, Irina V. Gorodetskaya
Writing – review & editing: Diogo Luís, Carla Gama, Cátia Gonçalves, José M. Castanheira, Alexandre M. Ramos, Michael Sprenger, Irina V. Gorodetskaya

atmospheric rivers (ARs) (Liberato, 2014; Smart, 2021; Stojanovic et al., 2021) that favored an explosive development of the cyclone (Ferreira et al., 2016).

An AR is “a long, narrow, and transient corridor of strong horizontal water vapor transport that is typically associated with a low-level jet stream ahead of the cold front of an extratropical cyclone” (Ralph et al., 2018). An average midlatitude AR has a width of about 850 km (varying from 300 to 1,000 km), an average length between 2,100 and 3,000 km, a vertical extent of 3 km, and a total water vapor flux of 5×10^8 kg s^{-1} (Gimeno et al., 2016; Neiman et al., 2008; Ralph et al., 2018; Ramos et al., 2015).

ARs represent the dominant pathway for horizontal water vapor transport in the midlatitudes (Ralph et al., 2018), making them key components of the global hydrological cycle. They can cause extreme precipitation with some areas in Western Europe having eight of the 10 largest rainfall events related to ARs (Lavers & Villarini, 2013) and with the most extreme precipitation days in the Iberian Peninsula (IP) associated with ARs (Ramos et al., 2015). The precipitation associated with this phenomenon is normally caused by the uplift of the moisture-rich air in the AR typically as part of the warm conveyor belt associated with an extratropical cyclone (Dacre et al., 2015; Eckhardt et al., 2004; Pfahl et al., 2014) or when it impinges on orographic barriers (Lavers & Villarini, 2013). In the latter case, the efficiency of the conversion of water vapor into precipitation depends on the angle with which the flow impinges on the local topography with more orthogonal impingement resulting in higher efficiency (Hu et al., 2017). Related to both extreme precipitation and compound events, ARs are also known to cause flood events across several European regions, including the Iberian Peninsula (Gimeno et al., 2016; Lavers & Villarini, 2013; Ramos et al., 2015). Study of the ARs and their impacts is highly relevant and urgent, especially as climate projections demonstrate an increase in intensity and frequency of ARs along the European coast, including the IP, during the 21st century (Ramos, Tomé, et al., 2016). This suggests an increased risk of intense precipitation and floods in these regions.

The identification of ARs is usually based on the integrated water vapor (IWV), which can be applied both to model outputs and satellite measurements (Neiman et al., 2008) or based on the vertically integrated horizontal water vapor transport (hereafter, integrated vapor transport, [IVT]) computed from reanalysis data sets (Lavers & Villarini, 2013; Lavers et al., 2012; Ramos et al., 2015, 2018). Multiple algorithms have been developed for the identification and tracking of ARs using various methodologies with different requirements (e.g., length, width, shape, intensity threshold, and time dependence) and applied to different meteorological variables and regions (Shields et al., 2018). The different criteria used by the AR algorithms result in a wide range of AR frequency, duration, and seasonality, which thus introduces some uncertainty into the analysis of AR impacts (Rutz et al., 2019).

Although the characteristics of ARs are relatively well known, many questions remain about their formation mechanisms and the sources of the water vapor present in ARs. The term “atmospheric river” can be interpreted as an existence of a continuous feed of moisture from the subtropics to the extratropics; however, the importance of both subtropical moisture sources and local moisture convergence, including continental moisture sources and recycling, have been shown by many studies (e.g., Algarra et al., 2020; Bao et al., 2006; Knippertz et al., 2013; Nusbaumer & Noone, 2018; Ramos, Nieto, et al., 2016; Terpstra et al., 2021). Further, Dacre et al. (2015) suggested that these structures are the footprints left behind by poleward traveling extratropical cyclones. In fact, they showed that warm and moist air in the warm sector of extratropical cyclones is swept up by the cold front, as it catches up with the warm front, narrowing the warm sector and creating an elongated band of high water vapor transport. Within this band, moisture is then transported northward as part of a warm conveyor belt of the extratropical cyclone (Dacre et al., 2015).

Thus, although there can be different moisture origins and drivers maintaining the ARs, they are typically related with extratropical cyclones and with the fronts associated with these cyclones. In the case of the ARs that affect the IP, they are related to extratropical cyclones that are formed in the North Atlantic and then move toward Europe and the IP. The activity of the extratropical cyclones is influenced by the position of blocking systems, which can result in a bifurcation of the storm tracks to north and south of their usual paths, and consequently, change the precipitation distribution over the continent (Sousa et al., 2017).

The main objective of this study is to better understand the governing mechanisms behind ARs affecting the IP and their contribution to precipitation. To achieve this goal, an AR identification algorithm was applied, aiming to identify the ARs that affected the IP during the 1979–2020 period. The characteristics and statistics of the events

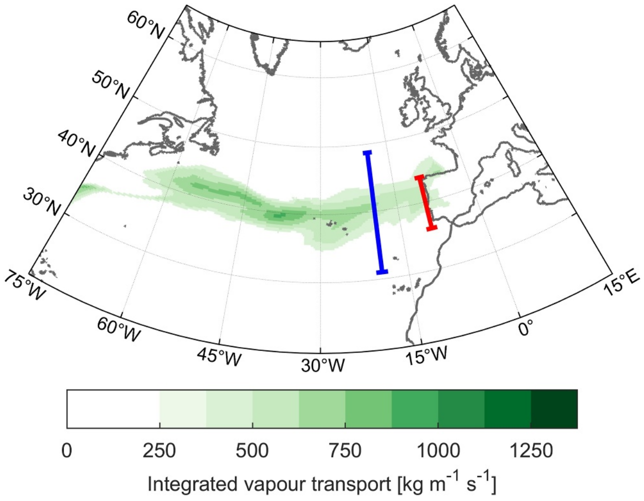

Figure 1. Example of a detected atmospheric river (AR) at 00:00 UTC 18 January 2013 (during the Storm Gong): integrated vapor transport intensity (kg m^{-1} s^{-1}, color shading) of the points considered as belonging to this AR and domains used for the detection of ARs (the coastal IP domain shown by red line and the Atlantic pre-IP domain shown by blue line).

identified as ARs are analyzed as well as their connection with the cold and warm fronts associated with extratropical cyclones and their relationship with precipitation over the IP.

This article is structured as follows: In Section 2, the AR algorithm, the data sets used, and the methodology are presented. In Section 3, three selected illustrative case studies of ARs that affected the IP are analyzed. In Section 4, a climatological analysis of the ARs that affected the IP between 1979 and 2020 is performed. Finally, the main conclusions are summarized in Section 5.

2. Data and Methods

2.1. AR Identification

In this study, we used the European Centre for Medium-Range Weather Forecasts (ECMWF) ERA5 reanalysis (Hersbach et al., 2020), with a spatial resolution of 0.25° × 0.25° (~31 km), during 1979–2020, in order to calculate the fields needed as input to an AR detection algorithm. Although ERA5 reanalysis is available with hourly temporal resolution, we used 6-hourly data for the identification of ARs, due to our focus on persistent AR cases (lasting at least 18 hr) and to increase algorithm efficiency. The ERA5 variables retrieved to identify ARs were the vertical integrals of eastward and northward water vapor flux (zonal and meridional components of IVT, respectively) at 00:00, 06:00, 12:00, and 18:00 UTC. Total precipitation and mean sea level pressure were also retrieved for the analysis presented in Sections 3 and 4.

To detect the ARs that affected the IP, an algorithm based on IVT was applied to ERA5, following the methodology by Lavers et al. (2012), Lavers and Villarini (2013), and Ramos et al. (2015) with some modifications. After the calculation of the total IVT fields and considering as ARs striking the IP those which cross the 9.5°W meridian between 36°N and 43.75°N latitudes (coastal IP domain, red line in Figure 1), the following methodology steps were applied to identify the ARs:

1. The maximum IVT at 12:00 UTC on each day from 1979 to 2020 in the coastal IP domain was found. An IVT threshold was computed using the 85th percentile of the maximum IVT distribution. The threshold obtained was 418 kg m^{-1} s^{-1} and this value was used as the threshold for the identification of ARs. The 85th percentile of the maximum IVT distribution at 12:00 UTC was chosen following the work of Lavers et al. (2012), where the authors showed that it corresponded to the IVT value of the most intense ARs.
2. The maximum IVT along the IP domain was calculated at each 6-hr time step. If the maximum IVT exceeded the IVT threshold, the maximum IVT location and time step were recorded.
3. For those time steps that exceeded the IVT threshold, the grid points that potentially belonged to an AR (hereafter, AR points) were identified. A grid point was classified as an AR point if its IVT value exceeded the IVT threshold and if it was connected to at least one AR point (to ensure the AR spatial continuity). An example of the points classified as AR points is shown in Figure 1.
4. A spatial criterion was applied to the identified points to determine if they have the minimum length necessary to be considered an AR. If a time step has 81 or more consecutive longitude points above the IVT threshold (80 intervals X 0.25° = 20°), that time step is considered an AR time step. Considering that at 40°N the length of a degree of longitude is ~85 km, then the minimum required length to be classified as an AR is, approximately, 1,700 km.
5. Furthermore, temporal criteria were applied to identify persistent ARs, that is, ARs that have at least 18 hr of duration (three 6-hr time steps). Hence, if an AR event occurred for three or more consecutive time steps, it was considered a persistent AR event and was flagged. Moreover, two persistent ARs were considered distinct events only if they were separated by more than 1 day. As the AR detection scheme uses an Eulerian framework, the assumption that two events are separated by more than 24 hr may allow two distinct objects to be identified as part of the same persistent AR event. Nevertheless, the 24-hr window ensures that all identified objects are associated with the same synoptic situation.

Although this AR algorithm is based mainly on the methodology described by Ramos et al. (2015), some differences exist in the definition of the IVT threshold in this work. Ramos et al. (2015) analyzed extreme precipitation events in the IP during the winter, so they used only the extended winter months (October–March) maximum IVT distribution for the calculation of the IVT threshold. In Ramos et al. (2018), the authors did a similar study during summer and used only the extended summer months (April–September) to compute the IVT threshold. Here, we use the maximum IVT distribution for the entire year (a single IVT threshold), which results in an IVT threshold lower (higher) than a winter (summer) based threshold. Therefore, in this study, we expect to detect a higher (lower) number of ARs than in a winter (summer) based study.

Applying the previous set of criteria, a total of 4,671 AR time steps affecting the IP in the period 1979–2020 were identified of which 3,810 corresponded to 580 distinct persistent AR events. In this study, only persistent ARs were considered in the analysis of results. The persistent AR events identified in this study are available in an AR detection catalog at https://doi.org/10.5281/zenodo.15120540 (Luís et al., 2025).

The same algorithm was also run for a new domain at 19.5°W and between 31°N and 48.75°N (the Atlantic pre-IP domain, blue line in Figure 1) but using the IVT threshold obtained for 9.5°W (the coastal IP domain) with the objective of identifying the AR time steps before the AR strikes the IP. After the identification of the ARs at 19.5°W (half the minimum length of the AR west of the IP), we retained only those ARs that also struck the IP at least during 3 consecutive time steps. This condition guarantees that a persistent AR at 19.5°W will be also a persistent AR at 9.5°W. Applying the AR detection algorithm to the Atlantic pre-IP domain allowed the identification of 3,102 new AR time steps, corresponding to the early stages of the ARs life cycle before reaching the IP. These additional AR time steps were only used in the analysis presented in Section 4.2, as only the AR time steps impacting the IP were analyzed in the remaining sections of the study.

2.2. Extratropical Fronts

To study the relationship between ARs and extratropical fronts, a slightly modified version of the front detection algorithm described by Jenkner et al. (2010) and Sprenger et al. (2017) was applied to ERA5 reanalysis with a spatial resolution of 0.5° × 0.5° during 1980–2019. The applied algorithm defines fronts as regions where the horizontal gradient of equivalent potential temperature (θ_e) at 700 hPa is higher than 4 K/100 km and the front exceed a minimum length of 500 km. Schemm et al. (2015) concluded that the methodology used by this algorithm is reliable in identifying fronts in strong baroclinic cases, such as the case of classical North Atlantic low-pressure systems that affect the IP. The identified fronts were divided by type into cold, warm, and indefinite fronts using an advection criterion. The indefinite category includes all frontal regions where the algorithm was not able to distinguish the type of front. An example of the identified fronts and respective type together with the θ_e and $\nabla\theta_e$ ERA5 fields used by the front detection algorithm is shown in Figures S1 and S2 in Supporting Information S1.

Using the location of frontal regions in ERA5, a search for the number of AR points that have a front in the proximity was performed for each persistent AR time step identified. It was considered that an AR point has a front in the vicinity if it is located at 2° or less of distance (following Ralph et al. (2004)). After performing this search for each time step and for each AR point, the AR points flagged with a front in proximity were summed and divided by the total number of AR points in that time step to calculate the fraction of AR points that have a front in their proximity. These calculations were repeated posteriorly considering only cold, warm, and indefinite fronts. It was assumed that an AR point could be in the proximity of more than one type of front simultaneously.

2.3. Precipitation in the Iberian Peninsula

The analysis of precipitation in the IP, including the contribution of ARs to precipitation, was based on three data sets: the global reanalysis, ERA5, and the regional observational gridded products, E-OBS, and Iberia01 (IB01). In this study, ERA5 hourly total precipitation values between 1979 and 2020 were analyzed over the region between latitudes 35°N and 45°N and longitudes 15°W and 5°E. The E-OBS gridded data set is from the European Climate Assessment & Dataset project network (Cornes et al., 2018), covering 1950 to the present with a daily temporal resolution. Total precipitation from the ensemble E-OBS data set, version 23.1e, was used (using the mean across the ensemble) for the period 1979–2020 with the same horizontal resolution as ERA5 (0.25° × 0.25°). Finally, the data set with the highest horizontal resolution, 0.1° × 0.1°, is IB01, which was created especially for the IP (Herrera et al., 2019). The IB01 also has daily temporal resolution and covers the period from 1979 to 2015 a total of 37 years within our study period.

To estimate ARs contribution to the total precipitation in the IP, the outputs of the AR detection algorithm described in Section 2.1 were used, namely the day of the event, the start and end time (i.e., 00:00, 06:00, 12:00, or 18:00 UTC), and the area affected by the AR event. For ERA5, the exact start time of the event was considered, and it was assumed that, after the period in which the event was detected by the algorithm, the precipitation persists over the IP for another 12 hr. On the other hand, E-OBS and IB01 have daily temporal resolution and follow different temporal approaches. For E-OBS, the daily precipitation over Spain on day n is the accumulated value from 07:00 UTC on day n to 07:00 UTC on day $n + 1$. For IB01, the accumulation period differs: precipitation is accumulated between 07:00 UTC on day $n - 1$ and 07:00 UTC on day n. Moreover, for data over Portugal, the 24-hr periods begin and end at 09:00 UTC. However, this distinction does not affect the analysis, as the ARs can only start at 00:00, 06:00, 12:00, or 18:00 UTC due to the input data used. Thus, regardless of whether the accumulation period is from 07:00 to 07:00 in Spain or from 09:00 to 09:00 in Portugal, the precipitation associated with ARs is captured consistently. Finally, considering the accumulated precipitation from the beginning to the end of the AR event and ensuring that the varying timeframes across data sets were aligned with the AR detection periods, an intersection was made with the area affected by the AR event in order to estimate the associated precipitation. The area affected by each AR event was determined as follows: for each 6-hr time step identified as AR, an AR mask was created containing the grid points belonging to the AR; then, for each AR event, the AR masks of that event were added up to obtain all grid points affected by the AR during the event. Precipitation outside the AR event mask was not included in the estimate of AR-associated precipitation.

This co-occurrence approach has some limitations particularly regarding precipitation that is spatially displaced from the area classified as an AR. One possible approach to minimizing this limitation is to use complex network techniques (Vallejo-Bernal et al., 2023). In this study, we opted for a simpler solution and the total area affected by the AR during the event was considered for precipitation attribution instead of the area of each time step. Nevertheless, some precipitation potentially associated with AR events fell outside the AR mask and was not considered in AR precipitation estimates. An example of this situation is shown and discussed in Section 3.1.

3. Analysis of Case Studies

3.1. Storm on 4–6 October 1979

The first event occurred in October 1979 and is an exemplar of an AR with a structure very close to the one typically presented as an AR illustration in textbooks. According to the AR intensity and impacts scale (Eiras-Barca et al., 2021; Ralph et al., 2019), this event was classified as a "strong" AR in some regions of the IP (AR3 category on a scale from AR1 to AR5). The analysis of IVT and sea level pressure fields for this event (Figure 2) shows that an extratropical cyclone was located in the North Atlantic, west of the British Isles, with a high-pressure ridge to the east (over Scandinavia and north-eastern Europe). Although an eastward displacement of the cyclone was blocked, the cold front associated with this extratropical cyclone moved cyclonically toward the warm front, sweeping the warm and moist air in the warm sector and consequently creating an elongated band of strong water vapor transport similarly to the mechanism described by Dacre et al. (2015).

Analyzing in more detail the relation between the AR and frontal regions, Figure 2a (18 hr before the landfall) shows the AR located between the cold and warm fronts with 73% of AR points in the proximity of a front (i.e., at 2° or less distance of a front). This percentage increased along the AR approach to the IP, as the cold front swept the AR warm and moist air toward the warm front. At the AR landfall (Figure 2b), 96% of AR points were near a front (79% in the proximity of a cold front and 43% near a warm front). During the AR lifetime, with the movement of the cold front, the AR width progressively decreased until 12 hr after the landfall (Figure 2c). After this time step, the algorithm does not detect an AR time step until 18 hr later (Figure 2d), when the IVT is still high, but with a shorter extent, affecting the southern part of the IP. According to the set of criteria listed in Section 2.1, this last time step is still considered to be part of the AR event. Thus, the AR event duration considered for precipitation analysis is from 5 October 1979, 06:00 UTC to 6 October 12:00 UTC.

The total precipitation amount accumulated over the IP during this event is shown in Figure 3. Both IB01 and ERA5 data sets show a similar spatial distribution with larger precipitation amounts over central and southern Portugal and over central Spain. However, the different data sets exhibit a very different magnitude of values.

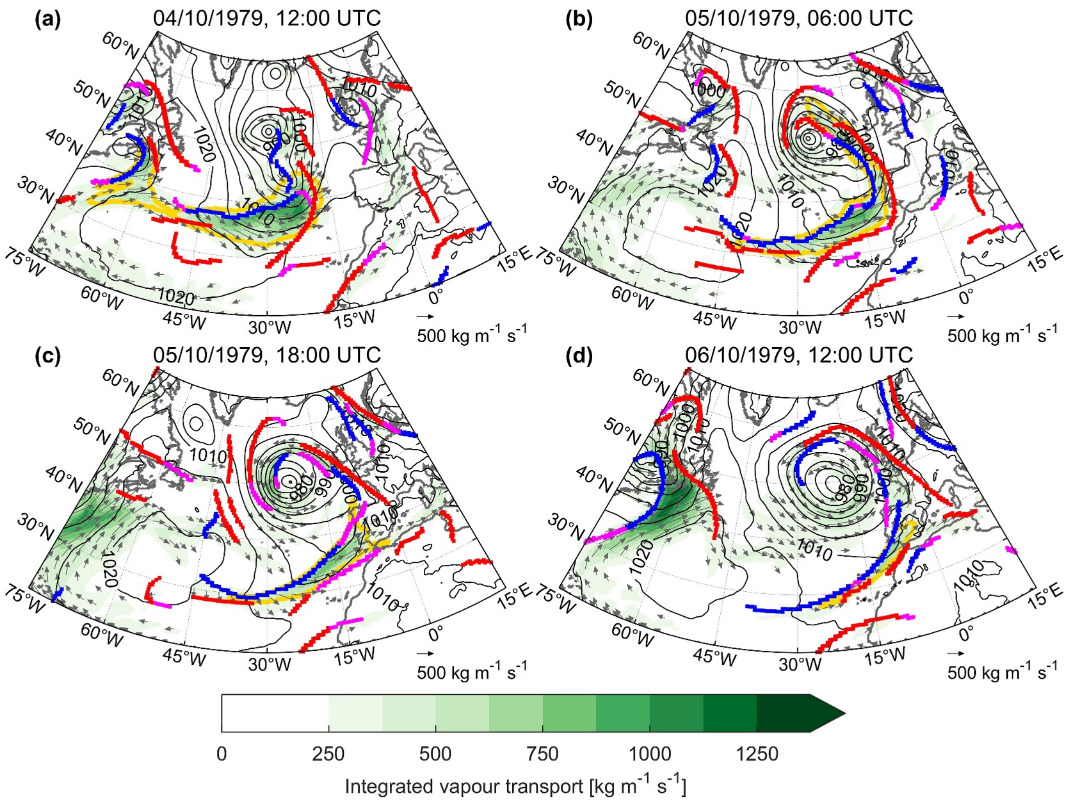

Figure 2. Integrated vapor transport direction (vectors) and intensity (kg m^{-1} s^{-1}, color shading), sea level pressure (hPa, contours), and cold, warm, and indefinite fronts (blue, red, and magenta points; respectively) at: (a) 12:00 UTC 4 October 1979, (b) 06:00 UTC 5 October 1979, (c) 18:00 UTC 5 October 1979, and (d) 12:00 UTC 6 October 1979. The orange contour shows the atmospheric river (AR) shape identified by the AR algorithm.

According to IB01 (Figure 3a), accumulated precipitation during the event has values above 50 mm in almost the entire Portuguese territory with maximums reaching over 120 mm in the central and southern regions. The central region of Spain reaches accumulated values above 110 mm. According to ERA5 reanalysis, the accumulated precipitation during this event is below 70 mm across the whole IP (Figure 3b). E-OBS data have also been analyzed (Figure S3a in Supporting Information S1), exhibiting maximum accumulated values ranging from 60 to

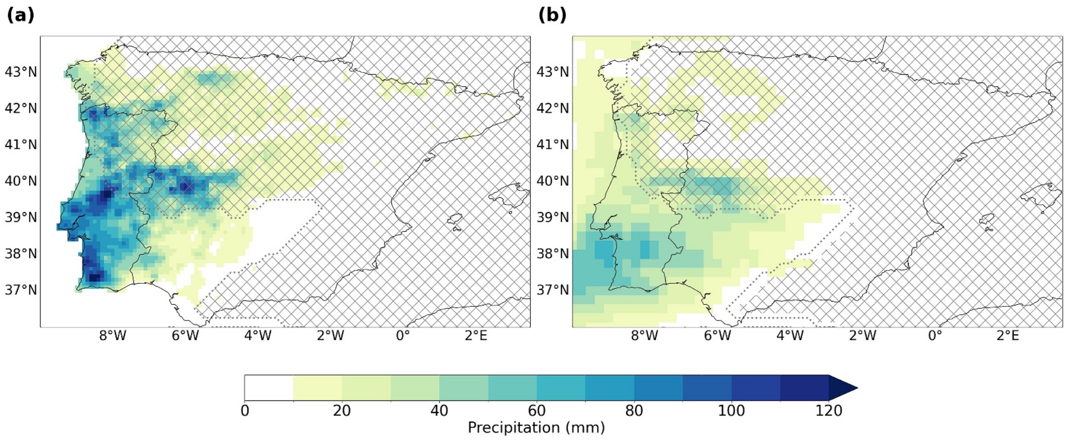

Figure 3. Accumulated precipitation (mm) over the IP during the October 1979 atmospheric river (AR) event (06:00 UTC 5 October 1979–12:00 UTC 6 October 1979): (a) IB01 data set and (b) ERA5 reanalysis. A gray dotted line shows the boundary of the AR mask identified by the AR algorithm (total area affected by the AR during the event duration) and the hatched area shows precipitation outside the AR mask.

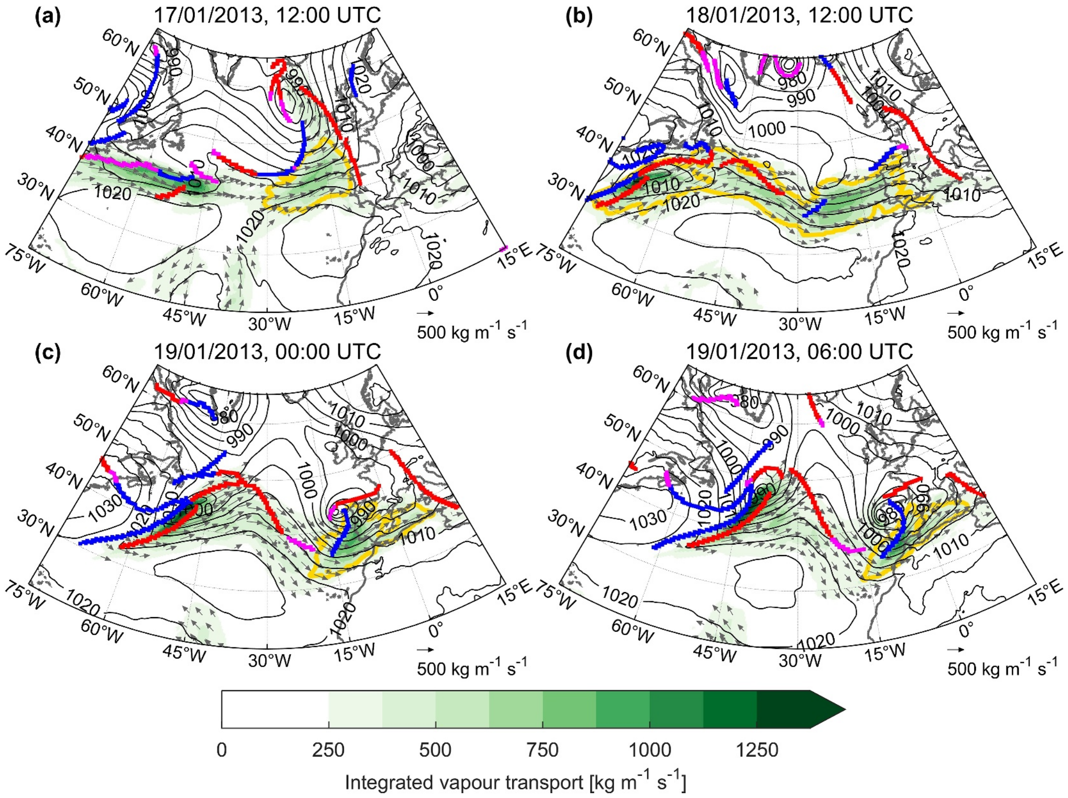

Figure 4. As in Figure 2, but at: (a) 12:00 UTC 17 January 2013, (b) 12:00 UTC 18 January 2013, (c) 00:00 UTC 19 January 2013, and (d) 06:00 UTC 19 January 2013.

80 mm over Portugal. These discrepancies in magnitude could be partly explained by the topographical differences captured by each data set. IB01, with its higher spatial resolution, is better suited to reflect the influence of complex terrain, where orographic effects are known to enhance precipitation. In contrast, the coarser resolution of ERA5 may smooth out these features, leading to lower precipitation estimates in areas where topography plays a significant role. Note that, for both data sets, the high precipitation accumulations over central Spain are outside the AR mask and are therefore not considered as associated with the AR. This is a limitation of the methodology used in this study and will likely cause an underestimation of the contribution of ARs to the total precipitation in the IP calculated in Section 4.3.

3.2. Storm Gong on 17–19 January 2013

The second event selected as a case study is Storm Gong, which affected Portugal on 18–19 January 2013. Gong was classified as an explosive cyclone, or a "bomb" with a very rapid strengthening supported by the presence of an atmospheric river over the North Atlantic. As Storm Gong moved with the associated AR toward the IP, it caused considerable socio-economic losses and fatalities (Liberato, 2014). This AR event reached the AR4 category ("extreme" AR) in several areas of the IP.

Although Gong cyclone's impact in terms of intensity of precipitation was the strongest in Portugal on 19 January 2013, the IP was being affected by an AR starting from 12:00 UTC on 17 January 2013 (Figure 4a). At this time, two extratropical cyclones, both associated with strong IVT, were found in the North Atlantic: a cyclone directly impacting the IP was situated west of the British Isles with well-developed meridionally oriented fronts and a second cyclone starting to develop and related to the future Storm Gong near the east coast of North America. In the following hours, IP continued to be affected by high IVTs with predominantly zonal (eastward) moisture transport (Figure 4b) enhanced when Storm Gong approached the IP and intensified (Figure 4c). Starting at 06:00 UTC on 18 January 2013, Gong underwent an explosive development when it was located north of the AR and between the Azores and the IP. The rapid strengthening of Gong was attributed to the southerly displacement

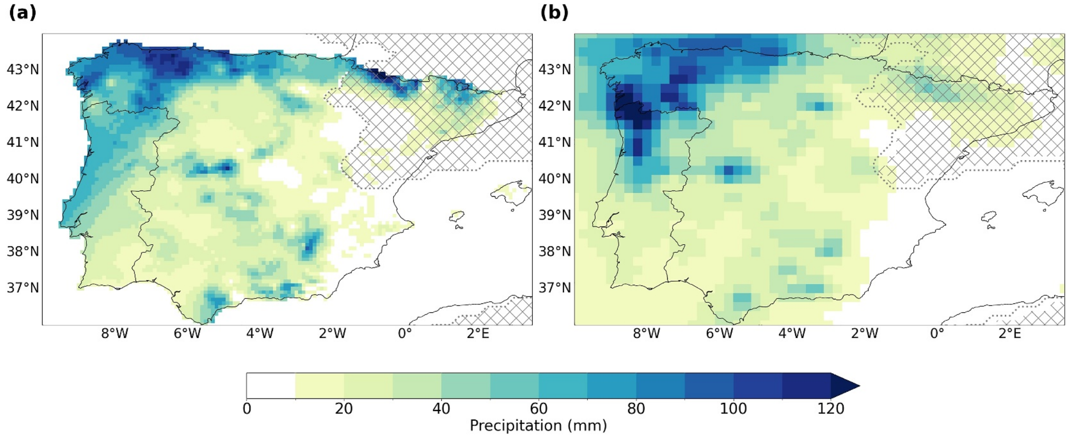

Figure 5. As in Figure 3, but for the Storm Gong atmospheric river event (12:00 UTC 17 January 2013–06:00 UTC 19 January 2013).

of the polar jet stream, the interaction of the high-level and low-level diabatically driven potential vorticity anomalies, and the extra moisture provided via the AR (Liberato, 2014). Near 00:00 UTC on 19 January 2013 (Figure 4c), when Storm Gong made landfall in the IP, it brought strong wind gusts and heavy precipitation (Liberato, 2014), but after inland penetration it began to dissipate. The last time step identified as an AR by the algorithm occurred at 06:00 UTC 19 January 2013 (Figure 4d) with a clear reduction in the AR length but with high IVT values in a narrow band between the cold and warm fronts. Throughout the event, a high-pressure system was situated south of the Azores, which favored the water vapor flux direction toward the IP (Figure 4).

Regarding the connection with extratropical fronts, this AR was mainly affected by the frontal systems associated with the two cyclones mentioned above: the cyclone located west of the British Isles and the Storm Gong. At the early stages of the AR life cycle, the AR was affected only by the fronts associated to the first cyclone. In Figure 4a, one can observe that at the landfall moment, the AR was between a warm front and a cold front associated to the cyclone west of the British Isles. Around 18:00 UTC on 17 January 2013, as Storm Gong and its fronts were moving faster to the east than the cyclone already affecting the IP, the high IVT zones of both cyclones began to merge into a zonal-oriented AR extending from the IP to near the coast of North America. Over the next 24 hr, Storm Gong advanced eastward toward the IP and the AR moved along with the storm while affecting the IP. After the landfall of Storm Gong (Figures 4c and 4d), the length of the AR diminished with the AR bounded by a cold front to the west and a warm front to the north.

This event had a significant impact on IP precipitation. Figure 5a, using IB01 data set, shows that the precipitation affected a large portion of the IP with the most intense precipitation found along the northern coast of Spain and in the Pyrenees mountains. In Portugal, maximum precipitation (between 40 and 70 mm) was found over central-western and northwestern Portugal, whereas total precipitation amounts accumulated in northern Spain and in the Pyrenees reached 100–120 mm. Although the Pyrenees lie outside the defined AR shape, the region still experienced significant precipitation. This suggests that, although the AR itself did not directly cover the Pyrenees, the broader moisture transport associated with the event likely contributed to the observed precipitation in this area. The presence of moist air outside the AR boundaries can still enhance precipitation, particularly in regions like the Pyrenees, where topographical effects play a crucial role in precipitation intensification.

Figure 5b shows precipitation based on the ERA5 reanalysis, where the maximum accumulated precipitation (>120 mm) is found in the northern coastal Portugal and Galicia regions. E-OBS shows precipitation spatial distribution and magnitude similar to the ERA5 (Figure S3b in Supporting Information S1). It is noteworthy that the maxima found along central and southern Spain in both IB01 and ERA5 data sets (Figure 5) are absent in E-OBS (Figure S3b in Supporting Information S1).

3.3. Storm Ana on 9–11 December 2017

The third case that we analyze in detail occurred on 10–11 December 2017 and was named Storm Ana. Heavy rain and strong winds associated with this storm affected most of the IP; however, the biggest impacts were recorded in

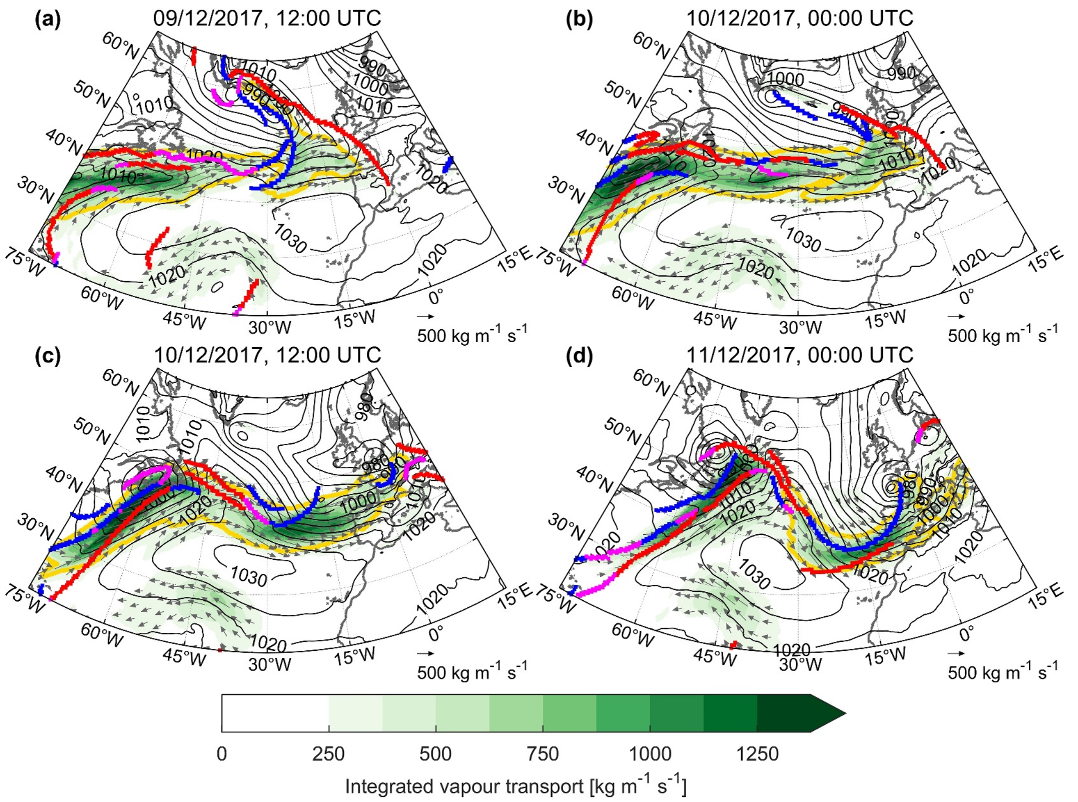

Figure 6. As in Figure 2, but at: (a) 12:00 UTC 9 December 2017, (b) 00:00 UTC 10 December 2017, (c) 12:00 UTC 10 December 2017, and (d) 00:00 UTC 11 December 2017.

the northwestern Iberia with wind gusts of over 160 km hr^{-1} registered in several stations in northern Spain and 232.0 mm of accumulated precipitation measured on 10 December at a station in Pontevedra (Galicia) (AEMET, 2017). This part of Iberia was impacted by conditions that reached the highest category on the AR-strength scale (AR5, an "exceptional" AR). This storm had a significant socioeconomic impact causing one fatality and more than 200 million euros in losses (Eiras-Barca et al., 2021).

As in the previous event (Section 3.2), the landfall of an AR preceded the arrival of Storm Ana to the IP. An AR affecting the IP was first detected at 12:00 UTC on 9 December 2017 (Figure 6a) with the AR located in the southern part of the warm sector of an extratropical cyclone in the North Atlantic pushed from the south by a high-pressure system situated over the Azores. Similar to the previous case in 2013, the AR in the beginning of its life cycle was in the precold frontal region (compare Figures 4a and 6a). During the early time steps identified as an AR, this synoptic configuration supported a strong zonal moisture transport between the two margins of the Atlantic Ocean (Figure 6b). On 10 December 2017, Storm Ana was formed around 45°N, 20°W–30°W through explosive cyclogenesis (AEMET, 2017). Between 10 December 2017, 12:00 UTC (Figure 6c) and 11 December 2017, 00:00 UTC (Figure 6d), the atmospheric pressure in the center of Ana dropped by 24 hPa in 12 hr (IPMA, 2017) when the storm was located on the northern edge of the AR. During this period, Storm Ana started to move southward, pushing the AR from the northern to the southern IP. On 11 December 2017, 00:00 UTC (Figure 6d), Ana reached its minimum pressure at its center (964 hPa), when it was located in the Bay of Biscay, and then continued its rapid movement toward France. The last time step identified as an AR occurred on 06:00 UTC 11 December 2017 with Storm Ana located over Brittany (France) and the AR affecting southern IP and the Balearic Islands.

In relation to the presence of fronts, like in the previous event, this AR was affected by the frontal systems associated with two extratropical cyclones. First, the AR was located between the cold and warm fronts associated with an extratropical cyclone south of Greenland (Figure 6a). In the following hours, the AR continued its eastward course, following the movement of the warm front. Around 12:00 UTC on 10 December 2017

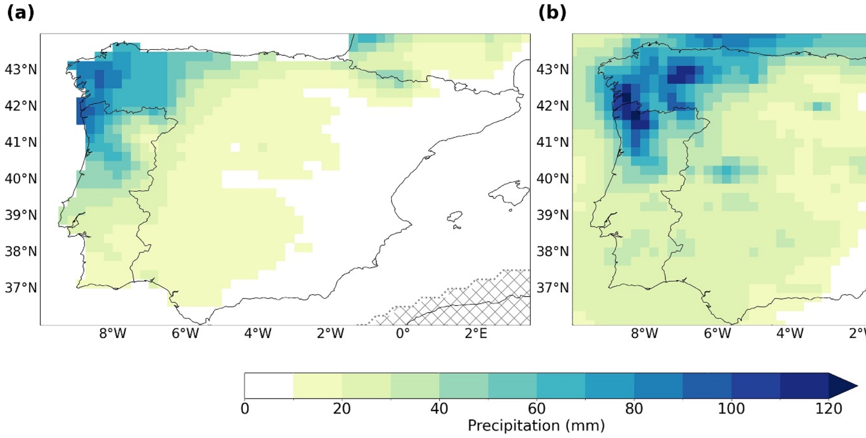

Figure 7. As in Figure 3, but for the Storm Ana atmospheric river event (12:00 UTC 9 December 2017–06:00 UTC 11 December 2017): (a) E-OBS data set and (b) ERA5 reanalysis.

(Figure 6c), a cold front associated to Storm Ana was formed to the north of the AR. With the storm movement, the very active cold front (AEMET, 2017) swept first the warm and moist air of the AR toward IP and then from the northern to the southern IP. In the last hours of the AR life cycle (Figure 6d), it was again between the cold and warm fronts of an extratropical cyclone (Ana) with the cold front almost catching up the warm front, thereby narrowing and elongating the AR before dissipation.

Figure 7 presents the accumulated precipitation over the IP for the AR associated with Storm Ana. Since IB01 data are not available for this event, we base our analysis on E-OBS and ERA5 data sets. Figure 7a, based on E-OBS, shows that the maximum accumulated precipitation for this event (between 90 and 100 mm) was mainly affecting northern Portugal and northwestern Spain. Important amounts of precipitation (40–80 mm) were also observed in Central Portugal and in the Pyrenees. ERA5 (Figure 7b) shows a similar pattern of the accumulated precipitation compared to E-OBS but with higher magnitudes (with maximum values above 120 mm). It also shows the existence of other maxima that were not identified by the E-OBS (such as in northern Spain, Cantabrian Mountains region). Overall, it is striking that the spatial pattern of the total accumulated precipitation for Storm Ana is very similar to the Storm Gong with the accumulated precipitation for this event affecting mostly the northwestern IP. Furthermore, this event occurred after a prolonged and severe drought in the Galicia region, and the precipitation associated with this AR was enough to fill water reservoirs in a single day (Eiras-Barca et al., 2021).

4. Climatological Analysis

4.1. Characteristics and Statistics of Iberian ARs

Following the case studies showing details of the ARs association with fronts and precipitation over the IP, we present a long-term analysis of the persistent ARs (identified as described in Section 2.1) affecting the IP between 1979 and 2020 based on ERA5 reanalysis.

During this 42-year period, the IP was affected by 580 persistent ARs corresponding to a mean value of 13.8 ± 2.8 ARs per year (Figure 8a). The minimum number of ARs in a year was reached in 2005 with only 7, and the maximum occurred in 2013 with 20 ARs. For comparison purposes, the AR algorithm was also applied to ECMWF's ERA-Interim reanalysis (Dee et al., 2011) for the period 1979–2018. Although fewer ARs were identified in ERA5 compared to ERA-Interim (with the latter showing an average of 15.0 ± 3.4 ARs per year based on the 40-year period; more details in Text S1 in Supporting Information S1), the interannual variability shows a good agreement between both reanalyses (Figure 8a).

Figure 8b shows the ERA5 monthly mean number of ARs that affected the IP in the 1979–2020 period and respective percentage of the AR total. A strong seasonal cycle is observed in the monthly frequency of ARs with the months of December (15.5%), October (14.0%), November (12.1%), and January (10.9%) being the months with more AR activity (together have more than half of the ARs). Most of the ARs occur in the extended winter months (66.9%) and the minimum in frequency of Iberian ARs occurs in April (4.1%). After April, a slight

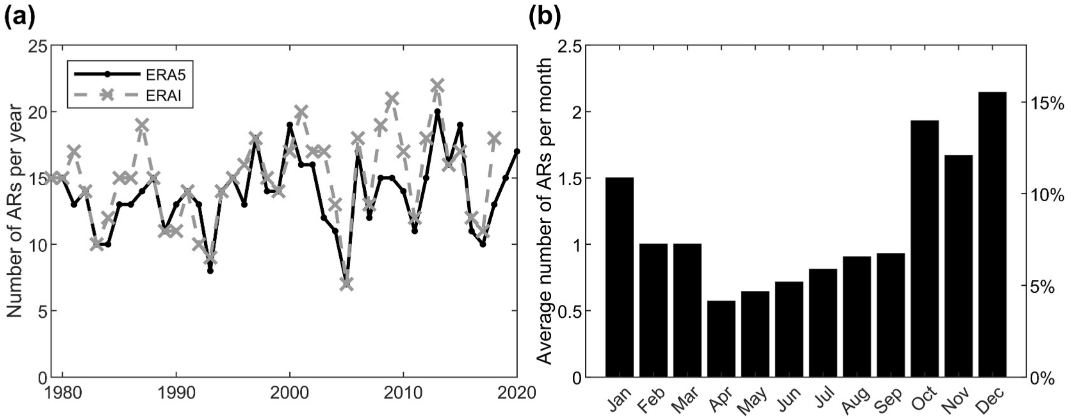

Figure 8. (a) Interannual variability of the number of persistent atmospheric rivers (ARs) that affected the IP computed with ERA5 (black line) and with ERA-Interim (dashed gray line), (b) seasonal variability of the number of ARs over the IP from 1979 to 2020 in ERA5.

increase in the AR activity per month is observed throughout the extended summer months, until October, when the number of ARs doubles compared with the previous month. The seasonal variability obtained agrees with the seasonal variability of the extended winter months shown in Ramos et al. (2015). Regarding the extended summer months, the increment in AR activity agrees with the results of Ramos et al. (2018), although in that study the minimum in the frequency of Iberian ARs occurs in June. Seasonal variability in ERA-Interim is similar to ERA5, though a small increase in AR activity is observed in March and the minimum is reached in May (Figure S4 in Supporting Information S1).

The ARs identified by the algorithm applied to ERA5 (at 6-hourly temporal resolution) affected the IP, on average, during 6.6 time steps (~39 hr) with approximately 75% of the ARs lasting between 18 and 48 hr and with 21.2% of cases having the minimum duration required to fulfill the persistence criteria (18 hr). In terms of zonal extension, the detected ARs had a mean zonal extension of 44° ± 16.7° of longitude (~3,750 ± 1,420 km) and with nearly half of the AR time steps having a zonal extension between 20° (~1,700 km) and 40° (~3,400 km).

Figure 9a shows the frequency of occurrence of AR events affecting the IP between 1979 and 2020. The maximum number of Iberian ARs is found at northwest of the IP and its frequency decreases toward south. As expected, the most affected region is the western coast of IP with an average of ~12 ARs per year in the north of Galicia and ~5 ARs per year in the southern parts of Portugal. In Figure 9b, the composite average of IVT during

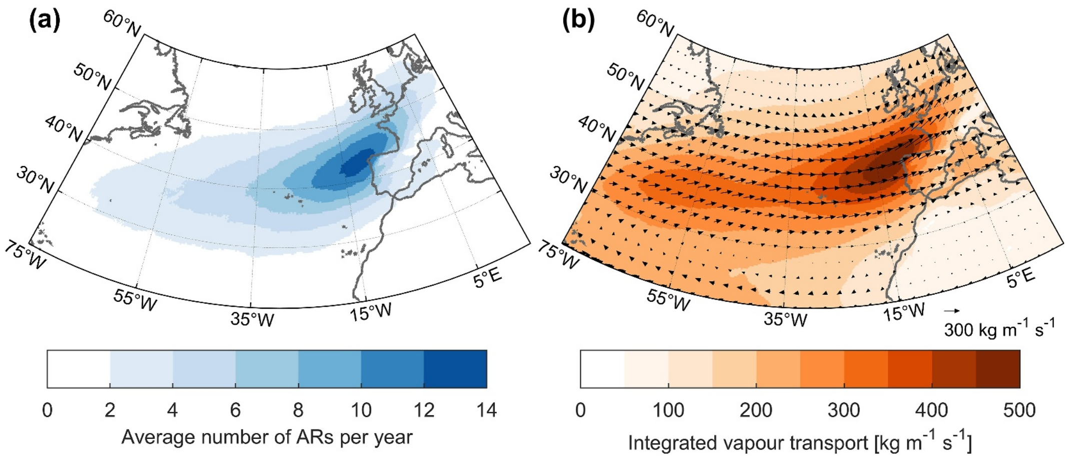

Figure 9. (a) Average number of atmospheric rivers (ARs) affecting the IP per year from 1979 to 2020 in ERA5, (b) Mean composites of ERA5 integrated vapor transport direction (vectors) and intensity (kg m^{-1} s^{-1}, color shading) during the occurrence of the ARs that affected the IP in the period 1979–2020.

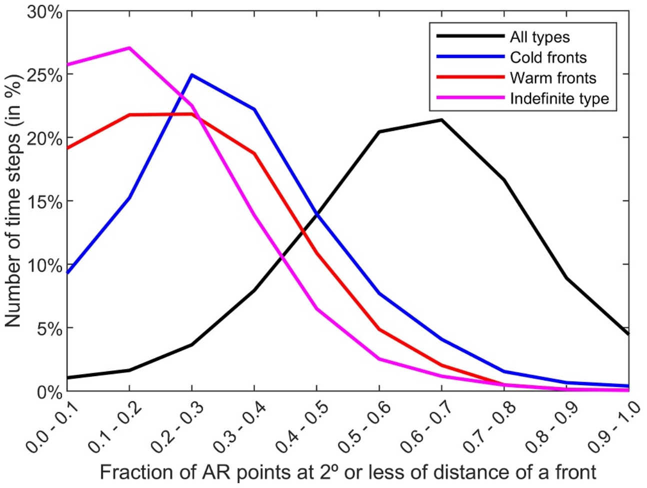

Figure 10. The fraction of atmospheric river points that have a front at 2° or less of distance, in the period from 1980 to 2019, divided into 0.1 bin intervals for all types of fronts (black line), cold fronts (blue line), warm fronts (red line), and indefinite type (magenta line).

AR events affecting the IP in the period 1979–2020 is shown. The IVT maxima are located over the ocean, northwest of the IP, which corroborates the results of Figure 9a. The IVT direction shows a westerly water vapor transport slightly tilted toward northeast. The pattern in Figure 9b is similar to the one shown in Figure 5b of Ramos et al. (2015) using the extended winter months in NCEP-NCAR reanalysis.

These results show that, although the small modifications to the AR algorithm, the Iberian AR characteristics and statistics obtained in this work are similar to the ones presented in previous studies (Eiras-Barca et al., 2016; Ramos et al., 2015, 2018) using different reanalyses. The alterations in the IVT threshold definition allowed the detection of more ARs without changing the characteristics of the identified structures. It is important to note that the previous studies on Iberian ARs focused mainly on the association with anomalous precipitation; although in this study, we are interested in all events regardless of their magnitude.

4.2. Relationship Between Extratropical Fronts and Iberian ARs

Next, we explored a statistical relationship between extratropical fronts and ARs affecting Iberia using all persistent AR time steps identified regardless of whether they were affecting the IP in that instant or not. For this purpose, the fraction of AR points with a front in its proximity was computed for each AR time step. As explained in Section 2.2, it was considered that an AR point has a front in its proximity if a front was identified at 2° or less of distance. The fraction value is between 0 and 1, where 0 means no fronts in the vicinity of the AR and 1 indicates that all AR points were near a front.

Figure 10 shows the frequency of AR time steps (% with respect to the total number of persistent AR time steps) as a function of the AR points fraction in the vicinity of a front of any type and, separately, by type of front. In case an AR point was in the vicinity of more than one type of front at the same time, that point was counted only once. The black curve in Figure 10 represents the fraction of AR points near all types of fronts and, as expected, shows higher values than the other curves that represent a single front type. The highest frequency of AR cases (~21%) had a fraction of 0.6–0.7 of its points in the proximity of a front. Approximately, 72% of the time steps had more than half of the AR points nearby a front (of any type) and in more than 91% of the cases, the fraction was larger than 1/3.

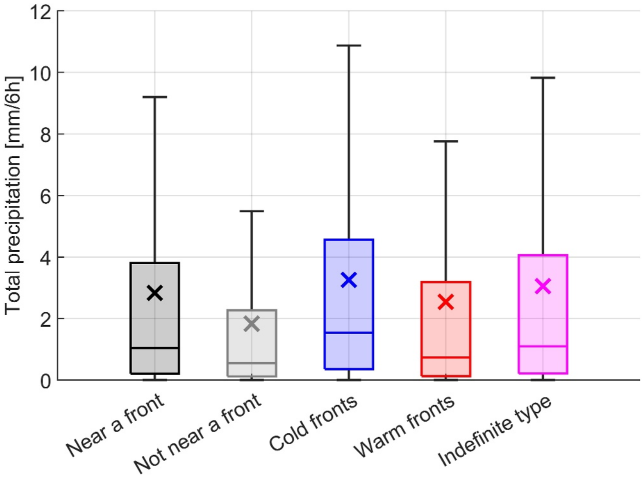

Figure 11. Boxplots of ERA5 total precipitation (mm/6 hr) at atmospheric river points found near a front of any type (black bar), not found near a front (gray bar), near a cold front (blue bar), near a warm front (red bar), and near a front of indefinite type (magenta bar). The mean values of each distribution are indicated by a cross. Outlier values are not shown.

Analyzing the relationship between extratropical fronts and Iberian ARs by type of front, Figure 10 shows that the AR points fraction near cold fronts is higher than near warm fronts: around 42% of the AR time steps had a fraction of AR points in the vicinity of a cold front superior to 1/3, whereas this percentage of cases for warm fronts is only ~30%. Moreover, some ARs were found near fronts of indefinite type.

Next, we analyzed the values of ERA5 precipitation for AR points near and not near a front (Figure 11). We found higher precipitation values in the AR points located in the vicinity of a front (median of 1.04 mm/6 hr) compared to the AR points not in the proximity of fronts (median of 0.55 mm/6 hr). This result is in line with previous studies on the attribution of precipitation to atmospheric phenomena at global scale (Konstali et al., 2024; Prein et al., 2023; Tsai et al., 2025) that found higher precipitation intensities during the co-occurrence of fronts and ARs. These studies did not distinguish between different types of fronts.

Our analysis shows greater precipitation values at AR points near cold frontal regions (median of 1.53 mm/6 hr) than near warm frontal regions (median of 0.73 mm/6 hr). Both the differences between the distributions of total precipitation at the AR points found near a front and not near a front and found near a cold front and near a warm front are statistically significant at the 1%

level (*p*-value obtained using the Mann-Whitney test). Higher precipitation values near cold frontal regions are consistent with previous studies showing that precipitation over oceanic storm-tracks is predominantly associated with cold fronts, whereas over continental regions in the Northern Hemisphere it tends to be linked to warm fronts (Catto et al., 2012). Given that many of the AR landfalls over the Iberian Peninsula occur close to the coastline, it is plausible that cold frontal dynamics, often associated with stronger uplift mechanisms, dominate in these cases enhancing precipitation rates when ARs and cold fronts co-occur. The stronger lifting mechanisms associated with cold fronts, combined with the enhanced moisture transport by ARs, can lead to more intense precipitation. In contrast, warm fronts are typically associated with more gradual lifting and weaker convection, which may explain the lower precipitation intensities observed.

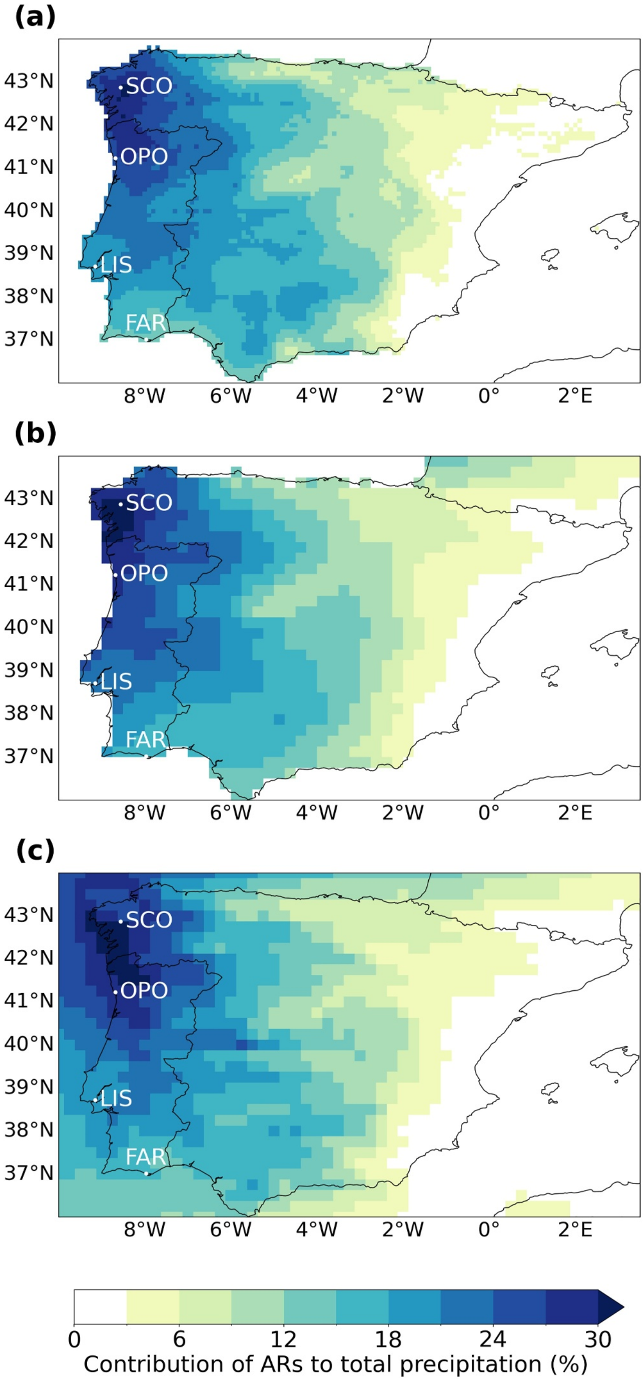

Figure 12. Atmospheric rivers contribution (%) to IP total precipitation based on: (a) IB01 data set during 1979–2015, (b) E-OBS data set during 1979–2020, and (c) ERA5 reanalysis during 1979–2020. SCO—Santiago de Compostela, OPO—Oporto, LIS—Lisbon, and FAR—Faro.

4.3. Precipitation Associated to Iberian ARs

Finally, we analyze the contribution of the ARs to precipitation over the IP. To obtain this contribution, the precipitation associated to each AR event (as defined in Section 2.3) was integrated over the entire period of study for each precipitation data set. In absolute terms, the maximum precipitation associated with ARs occurs in the northwest of the Iberian Peninsula regardless of the data set used (Figure S5 in Supporting Information S1). This is due to the highest frequency of the ARs landfalling in this region, maximum IVT, and orographic enhancement. Based on the ERA5 and IB01 data sets, the maximum absolute values occur in the north of Portugal near the Gerês mountain range (in the Peneda-Gerês National Park) where ARs contribute with roughly 640 mm (ERA5) or 550 mm (IB01) during an average year. Previous studies (Blamey et al., 2018; Gimeno et al., 2014) have shown already that mountainous regions, especially the slopes, are affected by precipitation associated with ARs. According to E-OBS, the maximum absolute value of precipitation associated with ARs (roughly 510 mm) occurs at the coast of Galicia (Spain), near Vigo and Pontevedra.

The IB01 regional product has the best spatial resolution among the three data sets, allowing, for example, a better assessment of the orographic enhancement of precipitation compared to E-OBS and ERA5 (Figure S6 in Supporting Information S1). However, this product has the most limited temporal coverage (ending in 2015).

Figure 12 shows the precipitation associated with ARs, as a percentage of the total annual precipitation, according to the three different data sets used in this study. The spatial distribution shown in these maps is very similar to the one of the total annual precipitation (Figure S6 in Supporting Information S1) except at the north of Spain (where, based on the IP01, the mean total annual precipitation reaches values higher than 1,500 mm near the Cantabrian and the Pyrenees mountain ranges, with ARs contributing less than 12% to this value). In relative terms, the highest ARs contribution to total precipitation occurs at the northwest coast of the IP between Santiago de Compostela (SCO) and Porto (OPO) where the mean total annual precipitation reaches values higher than 1,500 mm, with ARs contributing more than 24% to this value, regardless of the data set used. It should be noted that these values are derived from a 42 (ERA5 and E-OBS) or 37-year (IB01) timeframe, and in certain years, the contributions may exhibit significantly higher values than the average percentages shown here.

The relative mean contribution of ARs to total annual precipitation (Figure 12) shows a strong north-south gradient in Portugal and west-east in Spain. At the eastern coast of Spain, near the Mediterranean Sea, the contribution of ARs to total precipitation reaches its minimum level below 3%. Table 1 presents mean ARs contributions to annual precipitation at four cities located on the western IP distributed from north to south: Santiago de Compostela (SCO), Porto (OPO), Lisbon (LIS), and Faro (FAR).

Table 1
Contribution of Atmospheric Rivers to the Total Annual Precipitation

City	IB01 1979–2015	E-OBS 1979–2020	ERA5 1979–2020
SCO	29.5	31.3	26.7
OPO	26.3	28.2	27.5
LIS	19.9	23.2	19.9
FAR	13.5	16.2	16.6

Note. Mean annual ARs contribution to total precipitation (%), for Santiago de Compostela (SCO), Porto (OPO), Lisbon (LIS), and Faro (FAR), according to Iberia01 (1979–2015), E-OBS (1979–2020), and ERA5 (1979–2020) data sets.

According to these results, Santiago de Compostela, located about 40 km from the Atlantic Ocean, has the highest contribution of ARs to the total annual precipitation (ranging from 26.7% based on ERA5 to 31.1% based on E-OBS). Faro, in the Portuguese southern coast, has the lowest contribution ranging from 13.5% (IB01) to 16.6% (ERA5). It should be noted that the difference between the IB01 estimate and E-OBS and ERA5 ones for Faro cannot be explained by the different periods considered in the analysis, as shown in Tables S1 and S2 in Supporting Information S1. These values align with the results from Lavers and Villarini (2015), which attribute about 20%–30% of all precipitation in parts of Western Europe to ARs.

The significant contribution of ARs to the total annual precipitation in these cities shows, on the one hand, their important role in sustaining local water resources and, on the other hand, also raises awareness of the potential for enhanced risk of flooding and the need for resilient urban planning strategies.

5. Conclusions

In this work, an automatic AR detection algorithm was applied to IVT fields of ERA5 reanalysis for the period 1979–2020. The characteristics of persistent ARs (lasting at least 18 hr) affecting the IP, their relationship with extratropical fronts, and their associated precipitation were analyzed for the entire study period and, in more detail, for three case studies. Applying the same algorithm to ERA-Interim shows similar results with the climatology of the ARs affecting the IP in line with previous studies (Ramos et al., 2015, 2018). The use of ERA5, with higher spatial and temporal resolution, shows an advantage both in AR tracking, association of ARs with fronts and impact on IP precipitation.

The case studies show the presence of extratropical cyclones and associated fronts in different phases of the AR life cycle. In the October 1979 AR event, one can observe an AR located between the cold and warm fronts with the cold front moving cyclonically toward the warm front and sweeping the warm and moist air in the warm sector, creating an elongated band of high IVT values, as described by Dacre et al. (2015). In the other two case studies (storms Gong and Ana), the ARs were affected by two extratropical cyclones and respective frontal systems. In both cases, the second cyclone formed through explosive cyclogenesis north of the AR after the landfall of the initial cyclone. Long-term analysis during 1979–2020 showed that most of the ARs affecting Iberia are associated with extratropical cyclones and fronts. Furthermore, the analysis revealed that ARs are more frequently located closer to the cold front rather than the warm front. The analysis of the relationship between Iberian ARs and frontal regions also shows heavier precipitation located near fronts and higher values associated with cold fronts compared to warm fronts.

The effects of the ARs on the IP precipitation were studied using ERA5 and two gridded observational data sets (IB01 and E-OBS) available at daily temporal resolution. Persistent ARs showed a significant contribution to the total annual precipitation over IP with higher values in the northwestern region as well as in the mountainous regions. The magnitude of this contribution is higher in the north of the IP and decreases toward the south with persistent ARs being responsible for ∼30% of the annual precipitation in Santiago de Compostela, ∼27% in Porto, ∼20% in Lisbon, and ∼16% in Faro.

The results of this study demonstrate the key role that ARs play in the hydrological cycle of the Iberian Peninsula and their importance for sustainable management of water resources in the study region. The importance of extratropical fronts during an AR life cycle is also shown. This relationship needs to be further investigated, in particular, how it evolves from AR formation until AR depletion.

Conflict of Interest

The authors declare no conflicts of interest relevant to this study.

Data Availability Statement

E-OBS version 23.1e, ERA5, and ERA-Interim data produced by ECMWF are available through the Copernicus Climate Data Store (Copernicus Climate Change Service, 2020, 2023a, 2023b). The Iberia01 data are available from Gutiérrez et al. (2019). The atmospheric river detection catalog is available at https://doi.org/10.5281/zenodo.15120540 (Luís et al., 2025).

Acknowledgments

This work was supported by the Project ATLACE (CIRCNA/CAC/0273/2019, DOI: 10.54499/CIRCNA/CAC/0273/2019), funded by the Foundation for Science and Technology (FCT/MECI), in its State Budget component (OE). Thanks are also due to FCT/MECI for the financial support to CESAM (UID/50006 + LA/P/0094/2020, DOI: 10.54499/LA/P/0094/2020) and to CIIMAR (UIDB/04423/2020 and UIDP/04423/2020), through national funds, for the contract grants of C. Gama (2021.00732.CEECIND, DOI: 10.54499/2021.00732.CEECIND/CP1659/CT0006) and I. Gorodetskaya (2021.03140.CEECIND, DOI: 10.54499/2021.03140.CEECIND/CP1659/CT0005), and for PhD grant of D. Luís (2023.03574.BD, DOI: 10.54499/2023.03574.BD). A. M. Ramos was supported by the Helmholtz "Changing Earth—Sustaining our Future" program. Open access publication funding provided by FCT (b-on).

References

AEMET. (2017). Borrasca ana. Retrieved from https://www.aemet.es/es/conocermas/borrascas/2017-2018/estudios_e_impactos/ana

Algarra, I., Nieto, R., Ramos, A. M., Eiras-Barca, J., Trigo, R. M., & Gimeno, L. (2020). Significant increase of global anomalous moisture uptake feeding landfalling atmospheric rivers. *Nature Communications*, *11*(1), 5082. https://doi.org/10.1038/s41467-020-18876-w

Andrade, C., & Corte-Real, J. (2017). Assessment of the spatial distribution of continental-oceanic climate indices in the Iberian Peninsula. *International Journal of Climatology*, *37*(1), 36–45. https://doi.org/10.1002/joc.4685

Bao, J.-W., Michelson, S. A., Neiman, P. J., Ralph, F. M., & Wilczak, J. M. (2006). Interpretation of enhanced integrated water vapor bands associated with extratropical cyclones: Their formation and connection to tropical moisture. *Monthly Weather Review*, *134*(4), 1063–1080. https://doi.org/10.1175/MWR3123.1

Blamey, R. C., Ramos, A. M., Trigo, R. M., Tomé, R., & Reason, C. J. C. (2018). The influence of atmospheric rivers over the South Atlantic on winter rainfall in South Africa. *Journal of Hydrometeorology*, *19*(1), 127–142. https://doi.org/10.1175/JHM-D-17-0111.1

Cardoso Pereira, S., Marta-Almeida, M., Carvalho, A. C., & Rocha, A. (2019). Extreme precipitation events under climate change in the Iberian Peninsula. *International Journal of Climatology*, *40*(2), 1255–1278. https://doi.org/10.1002/joc.6269

Catto, J. L., Jakob, C., Berry, G., & Nicholls, N. (2012). Relating global precipitation to atmospheric fronts. *Geophysical Research Letters*, *39*(10), L10805. https://doi.org/10.1029/2012GL051736

Copernicus Climate Change Service. (2020). E-OBS daily gridded meteorological data for Europe from 1950 to present derived from in-situ observations [Dataset]. *Copernicus Climate Change Service (C3S) Climate Data Store (CDS)*. https://doi.org/10.24381/CDS.151D3EC6

Copernicus Climate Change Service. (2023a). ERA5 hourly data on single levels from 1940 to present [Dataset]. *Copernicus Climate Change Service (C3S) Climate Data Store (CDS)*. https://doi.org/10.24381/CDS.ADBB2D47

Copernicus Climate Change Service. (2023b). ERA-Interim global atmospheric reanalysis [Dataset]. *Copernicus Climate Change Service (C3S) Climate Data Store (CDS)*. https://doi.org/10.24381/CDS.F2F5241D

Cornes, R. C., van der Schrier, G., van den Besselaar, E. J. M., & Jones, P. D. (2018). An ensemble version of the E-OBS temperature and precipitation data sets. *Journal of Geophysical Research: Atmospheres*, *123*(17), 9391–9409. https://doi.org/10.1029/2017JD02820

Dacre, H., Clark, P., Martinez-Alvarado, O., Stringer, M., & Lavers, D. (2015). How do atmospheric rivers form? *Bulletin of the American Meteorological Society*, *96*(8), 1243–1255. https://doi.org/10.1175/BAMS-D-14-00031.1

Dee, D. P., Uppala, S. M., Simmons, A. J., Berrisford, P., Poli, P., Kobayashi, S., et al. (2011). The ERA-Interim reanalysis: Configuration and performance of the data assimilation system. *Quarterly Journal of the Royal Meteorological Society*, *137*(656), 553–597. https://doi.org/10.1002/qj.828

Eckhardt, S., Stohl, A., Wernli, H., James, P., Forster, C., & Spichtinger, N. (2004). A 15-year climatology of warm conveyor belts. *Journal of Climate*, *17*(1), 218–237. https://doi.org/10.1175/1520-0442(2004)017<0218:AYCOWC>2.0.CO;2

Eiras-Barca, J., Brands, S., & Miguez-Macho, G. (2016). Seasonal variations in North Atlantic atmospheric river activity and associations with anomalous precipitation over the Iberian Atlantic margin. *Journal of Geophysical Research: Atmospheres*, *121*(2), 931–948. https://doi.org/10.1002/2015JD023379

Eiras-Barca, J., Ramos, A. M., Algarra, I., Vázquez, M., Dominguez, F., Macho, M.-, et al. (2021). European west coast atmospheric rivers: A scale to characterize strength and impacts. *Weather and Climate Extremes*, *31*, 100305. https://doi.org/10.1016/j.wace.2021.100305

Ferreira, J. A., Liberato, M. L. R., & Ramos, A. M. (2016). On the relationship between atmospheric water vapour transport and extra-tropical cyclones development. *Physics and Chemistry of the Earth*, *94*, 56–65. https://doi.org/10.1016/j.pce.2016.01.001

Gimeno, L., Dominguez, F., Nieto, R., Trigo, R. M., Drumond, A., Reason, C. J. C., et al. (2016). Major mechanisms of atmospheric moisture transport and their role in extreme precipitation events. *Annual Reviews of Environment and Resources*, *41*(1), 117–141. https://doi.org/10.1146/annurev-environ-110615-085558

Gimeno, L., Nieto, R., Vázquez, M., & Lavers, D. A. (2014). Atmospheric rivers: A mini-review. *Frontiers in Earth Science*, *2*, 1–6. https://doi.org/10.3389/feart.2014.00002

Gutiérrez, J. M., Herrera, S., Cardoso, R. M., Soares, P. M. M., Espírito-Santo, F., & Viterbo, P. (2019). Iberia01: Daily gridded (0.1° resolution) dataset of precipitation and temperatures over the Iberian Peninsula [Dataset]. *Digital.CSIC*. https://doi.org/10.20350/DIGITALCSIC/8641

Herrera, S., Margarida Cardoso, R., Matos Soares, P., Espírito-Santo, F., Viterbo, P., & Gutiérrez, J. M. (2019). Iberia01: A new gridded dataset of daily precipitation and temperatures over Iberia. *Earth System Science Data*, *11*(4), 1947–1956. https://doi.org/10.5194/essd-11-1947-2019

Hersbach, H., Bell, B., Berrisford, P., Hirahara, S., Horányi, A., Muñoz-Sabater, J., et al. (2020). The ERA5 global reanalysis. *Quarterly Journal of the Royal Meteorological Society*, *146*(730), 1999–2049. https://doi.org/10.1002/qj.3803

Hu, H., Dominguez, F., Wang, Z., Lavers, D. A., Zhang, G., & Ralph, F. M. (2017). Linking atmospheric river hydrological impacts on the U.S. west coast to Rossby wave breaking. *Journal of Climate*, *30*(9), 3381–3399. https://doi.org/10.1175/JCLI-D-16-0386.1

IPMA. (2017). Passagem da Tempestade Ana a norte da Península Ibérica. Retrieved from https://www.ipma.pt/pt/media/noticias/news.detail.jsp?f=/pt/media/noticias/arquivo/2017/tempestade-ana.html

Jenkner, J., Sprenger, M., Schwenk, I., Schwierz, C., Dierer, S., & Leuenberger, D. (2010). Detection and climatology of fronts in a high-resolution model reanalysis over the Alps. *Meteorological Applications*, *17*(1), 1–18. https://doi.org/10.1002/met.142

Knippertz, P., Wernli, H., & Gläser, G. (2013). A global climatology of tropical moisture exports. *Journal of Climate*, *26*(10), 3031–3045. https://doi.org/10.1175/JCLI-D-12-00401.1

Konstali, K., Spensberger, C., Spengler, T., & Sorteberg, A. (2024). Global attribution of precipitation to weather features. *Journal of Climate*, *37*(4), 1181–1196. https://doi.org/10.1175/JCLI-D-23-0293.1

Lavers, D. A., & Villarini, G. (2013). The nexus between atmospheric rivers and extreme precipitation across Europe. *Geophysical Research Letters*, *40*(12), 3259–3264. https://doi.org/10.1002/grl.50636

Lavers, D. A., & Villarini, G. (2015). The contribution of atmospheric rivers to precipitation in Europe and the United States. *Journal of Hydrology*, *522*, 382–390. https://doi.org/10.1016/j.jhydrol.2014.12.010

Lavers, D. A., Villarini, G., Allan, R. P., Wood, E. F., & Wade, A. J. (2012). The detection of atmospheric rivers in atmospheric reanalyses and their links to British winter floods and the large-scale climatic circulation. *Journal of Geophysical Research*, *117*(D20), D20106. https://doi.org/10.1029/2012JD018027

Liberato, M. L. R. (2014). The 19 January 2013 windstorm over the North Atlantic: Large-scale dynamics and impacts on Iberia. *Weather and Climate Extremes*, *5*(1), 16–28. https://doi.org/10.1016/j.wace.2014.06.002

Liberato, M. L. R., Pinto, J. G., Trigo, I. F., & Trigo, R. M. (2011). Klaus - An exceptional winter storm over northern Iberia and southern France. *Weather*, *66*(12), 330–334. https://doi.org/10.1002/wea.755

Liberato, M. L. R., Pinto, J. G., Trigo, R. M., Ludwig, P., Ordóñez, P., Yuen, D., & Trigo, I. F. (2013). Explosive development of winter storm Xynthia over the subtropical North Atlantic Ocean. *Natural Hazards and Earth System Sciences*, *13*(9), 2239–2251. https://doi.org/10.5194/nhess-13-2239-2013

Luís, D., Castanheira, J. M., Ramos, A. M., & Gorodetskaya, I. (2025). Iberian atmospheric river detection catalogue based on ERA5 reanalysis data [Dataset]. *Zenodo*. https://doi.org/10.5281/zenodo.15120540

Neiman, P. J., Ralph, F. M., Wick, G. A., Lundquist, J. D., & Dettinger, M. D. (2008). Meteorological characteristics and overland precipitation impacts of atmospheric rivers affecting the west coast of North America based on eight years of SSM/I satellite observations. *Journal of Hydrometeorology*, *9*(1), 22–47. https://doi.org/10.1175/2007JHM855.1

Nusbaumer, J., & Noone, D. (2018). Numerical evaluation of the modern and future origins of atmospheric river moisture over the west coast of the United States. *Journal of Geophysical Research: Atmospheres*, *123*(12), 6423–6442. https://doi.org/10.1029/2017JD028081

Parracho, A. C., Melo-Gonçalves, P., & Rocha, A. (2016). Regionalisation of precipitation for the Iberian Peninsula and climate change. *Physics and Chemistry of the Earth*, *94*, 146–154. https://doi.org/10.1016/j.pce.2015.07.004

Pfahl, S., Madonna, E., Boettcher, M., Joos, H., & Wernli, H. (2014). Warm conveyor belts in the ERA-Interim dataset (1979–2010). Part II: Moisture origin and relevance for precipitation. *Journal of Climate*, *27*(1), 27–40. https://doi.org/10.1175/JCLI-D-13-00223.1

Prein, A. F., Mooney, P. A., & Done, J. M. (2023). The multi-scale interactions of atmospheric phenomenon in mean and extreme precipitation. *Earth's Future*, *11*(11), e2023EF003534. https://doi.org/10.1029/2023EF003534

Ralph, F. M., Dettinger, M. D., Cairns, M. M., Galarneau, T. J., & Eylander, J. (2018). Defining 'atmospheric river': How the glossary of meteorology helped resolve a debate. *Bulletin of the American Meteorological Society*, *99*(4), 837–839. https://doi.org/10.1175/BAMS-D-17-0157.1

Ralph, F. M., Neiman, P. J., & Wick, G. A. (2004). Satellite and CALJET aircraft observations of atmospheric rivers over the eastern north Pacific Ocean during the winter of 1997/98. *Monthly Weather Review*, *132*(7), 1721–1745. https://doi.org/10.1175/1520-0493(2004)132<1721:sacaoo>2.0.co;2

Ralph, F. M., Rutz, J. J., Cordeira, J. M., Dettinger, M., Anderson, M., Reynolds, D., et al. (2019). A scale to characterize the strength and impacts of atmospheric rivers. *Bulletin of the American Meteorological Society*, *100*(2), 269–289. https://doi.org/10.1175/BAMS-D-18-0023.1

Ramos, A. M., Martins, M. J., Tomé, R., & Trigo, R. M. (2018). Extreme precipitation events in summer in the Iberian Peninsula and its relationship with atmospheric rivers. *Frontiers in Earth Science*, *6*, 110. https://doi.org/10.3389/feart.2018.00110

Ramos, A. M., Nieto, R., Tomé, R., Gimeno, L., Trigo, R. M., Liberato, M. L. R., & Lavers, D. A. (2016). Atmospheric rivers moisture sources from a Lagrangian perspective. *Earth System Dynamics*, *7*(2), 371–384. https://doi.org/10.5194/esd-7-371-2016

Ramos, A. M., Tomé, R., Trigo, R. M., Liberato, M. L. R., & Pinto, J. G. (2016). Projected changes in atmospheric rivers affecting Europe in CMIP5 models. *Geophysical Research Letters*, *43*(17), 9315–9323. https://doi.org/10.1002/2016GL070634

Ramos, A. M., Trigo, R. M., Liberato, M. L., & Tomé, R. (2015). Daily precipitation extreme events in the Iberian Peninsula and its association with atmospheric rivers. *Journal of Hydrometeorology*, *16*(2), 579–597. https://doi.org/10.1175/JHM-D-14-0103.1

Rutz, J. J., Shields, C. A., Lora, J. M., Payne, A. E., Guan, B., Ullrich, P., et al. (2019). The atmospheric river tracking method intercomparison project (ARTMIP): Quantifying uncertainties in atmospheric river climatology. *Journal of Geophysical Research: Atmospheres*, *124*(24), 13777–13802. https://doi.org/10.1029/2019JD030936

Schemm, S., Rudeva, I., & Simmonds, I. (2015). Extratropical fronts in the lower troposphere–global perspectives obtained from two automated methods. *Quarterly Journal of the Royal Meteorological Society*, *141*(690), 1686–1698. https://doi.org/10.1002/qj.2471

Serrano, A., García, J., Mateos, V. L., Cancillo, M. L., & Garrido, J. (1999). Monthly modes of variation of precipitation over the Iberian Peninsula. *Journal of Climate*, *12*(9), 2894–2919. https://doi.org/10.1175/1520-0442(1999)012<2894:MMOVOP>2.0.CO;2

Shields, C. A., Rutz, J. J., Leung, L.-Y., Ralph, F. M., Wehner, M., Kawzenuk, B., et al. (2018). Atmospheric river tracking method intercomparison project (ARTMIP): Project goals and experimental design. *Geoscientific Model Development*, *11*(6), 2455–2474. https://doi.org/10.5194/gmd-11-2455-2018

Smart, D. (2021). Storm Filomena 8 January 2021. *Weather*, *76*(3), 98–99. https://doi.org/10.1002/wea.3950

Sousa, P. M., Trigo, R. M., Barriopedro, D., Soares, P. M. M., Ramos, A. M., & Liberato, M. L. R. (2017). Responses of European precipitation distributions and regimes to different blocking locations. *Climate Dynamics*, *48*(3–4), 1141–1160. https://doi.org/10.1007/s00382-016-3132-5

Sprenger, M., Fragkoulidis, G., Binder, H., Croci-Maspoli, M., Graf, P., Grams, C. M., et al. (2017). Global climatologies of Eulerian and Lagrangian flow features based on ERA-Interim. *Bulletin of the American Meteorological Society*, *98*(8), 1739–1748. https://doi.org/10.1175/BAMS-D-15-00299.1

Stewart, S. R. (2018). National Hurricane Center, tropical cyclone report, Hurricane Ophelia, (AL172017).

Stojanovic, M., Gonçalves, A., Sorí, R., Vázquez, M., Ramos, A. M., Nieto, R., et al. (2021). Consecutive extratropical cyclones Daniel, Elsa and Fabien, and their impact on the hydrological cycle of mainland Portugal. *Water (Switzerland)*, *13*(11), 1476. https://doi.org/10.3390/w13111476

Terpstra, A., Gorodetskaya, I. V., & Sodemann, H. (2021). Linking sub-tropical evaporation and extreme precipitation over east Antarctica: An atmospheric river case study. *Journal of Geophysical Research: Atmospheres*, *126*(9), e2020JD033617. https://doi.org/10.1029/2020JD033617

Trigo, R. M., Pozo-Vázquez, D., Osborn, T. J., Castro-Díez, Y., Gámiz-Fortis, S., & Esteban-Parra, M. J. (2004). North Atlantic oscillation influence on precipitation, river flow and water resources in the Iberian Peninsula. *International Journal of Climatology*, *24*(8), 925–944. https://doi.org/10.1002/joc.1048

Trigo, R. M., Valente, M. A., Trigo, I. F., Miranda, P. M. A., Ramos, A. M., Paredes, D., & García-Herrera, R. (2008). The impact of North Atlantic wind and cyclone trends on European precipitation and significant wave height in the Atlantic, trends and directions in climate research. *Annals of the New York Academy of Sciences*, *1146*(1), 212–234. https://doi.org/10.1196/annals.1446.014

Tsai, W. M., Duan, S., O'Brien, T. A., Catto, J. L., Ullrich, P. A., Zhou, Y., et al. (2025). Co-occurring atmospheric features and their contributions to precipitation extremes. *Journal of Geophysical Research: Atmospheres*, *130*(5), e2024JD041687. https://doi.org/10.1029/2024JD041687

Vallejo-Bernal, S. M., Wolf, F., Boers, N., Traxl, D., Marwan, N., & Kurths, J. (2023). The role of atmospheric rivers in the distribution of heavy precipitation events over North America. *Hydrology and Earth System Sciences*, *27*(14), 2645–2660. https://doi.org/10.5194/hess-27-2645-2023